$M\alpha$- and $M\beta$-satellite x-ray emission induced by electron impact on rhenium

Alejo Carreras,[1] Gustavo Castellano,[1] Jorge Trincavelli,[1] Silvina Segui,[1]
María del Rosario Torres Deluigi,[2] and Silvina Limandri[1,*]

[1]*Instituto de Física Enrique Gaviola, Facultad de Matemática, Astronomía, Física y Computación, Universidad Nacional de Córdoba, Córdoba, Argentina*

[2]*Departamento de Física, Universidad Nacional de San Luis–Instituto de Química de San Luis, San Luis, Argentina*

(Received 6 December 2024; accepted 18 April 2025; published xxxxxxxxxx)

Detailed expressions for satellite intensities have been carefully developed, taking into account Coster-Kronig single and double spectator hole states, and shake-up and shake-off events. The energies corresponding to satellite emissions originating from $M_{4,5}$ vacancies can be classified according to their shift from the $M\alpha$ and $M\beta$ parent peaks; for the specific example of rhenium, this approach enabled to analyze the intensity ratio associated with each energy region. These satellite emission energies and intensity ratios are also obtained experimentally for rhenium, after a parameter optimization routine developed previously, applied to a set of x-ray spectra induced by electron irradiation on a solid target, and acquired by means of a wavelength-dispersive spectrometer. These experimental data are compared to those assessed from the analytical expressions derived.

DOI: 10.1103/PhysRevA.00.002800

I. INTRODUCTION

The x-ray emission of characteristic (or diagram) lines is usually accompanied by structures called satellite lines whose energies cannot be inferred from the differences between two atomic levels involved in the decay. These satellite structures, which may appear on either side of the main peak, originate in different phenomena and may provide information about a variety of processes, such as electronic correlation, excitation dynamics, relaxation, atomic structure, and chemical environment of the emitting atom [1].

Among the satellite structures appearing in the low-energy region can be mentioned those originating in radiative Auger transitions [2] or decays from molecular orbitals [3]. Satellite lines bearing energies higher than the main emission are related to transitions from multiple vacancy states, the outer of them behaving as spectator holes [4]. When the incident projectile is an electron, these additional vacancies mainly arise from Coster-Kronig (CK) and Auger (AU) transitions or as a consequence of shake-up and shake-off (SH) processes [5]. The prediction of these phenomena may provide clues about the adequate description of electron states in atoms. As an example of such an attempt, the multiconfiguration Dirac-Hartree-Fock method is used in the assessment of manganese $K\alpha$ and $K\beta$ characteristic energies, shake-off probabilities and Auger rates [6], and also to calculate the scandium transition energies and relative probabilities of the diagram and shake-off satellite lines [7].

AU events are nonradiative transitions in which an inner-shell vacancy is filled involving the ejection of an outer-shell electron. When this relaxation occurs within sublevels of one shell, this mechanism is referred to as the CK transition. For the L shell, these transitions have deserved a number of experimental studies [8–19] as well as theoretical analyses [20,21]; however, information about the M-shell CK coefficients is seldom found in the literature [22]. Regarding shake processes, they involve the creation of a vacancy as a consequence of an electron ejection (shake-off) or excitation to a quasifree level (shake-up), as a result of the shaking of the atomic orbits caused by a sudden change in the potential field in the atom [23]. In this case, a few experimental reports exist for some elements, usually noble gases [24,25], and scarce theoretical calculations, within the relativistic and nonrelativistic sudden approximation framework [26–28].

Many applications have subsequently taken advantage of the presence of satellite emissions in experiments based on characteristic x-ray emission induced by different excitation sources [29]. In geochronology, the proper description of these transitions may be crucial [30], particularly in the analysis of monazites [31]. The high-temperature superconductor $YBa_2Cu_3O_{7-\delta}$ (critical temperature around 93 K) can also be mentioned within these examples: the δ oxygen deficiency or excess affects its superconducting properties, and can be analyzed by examining the O-K satellite structure [32]. Concerning the assessment of the redox conditions of rock formation, the estimation of the three manganese valence states in mineral objects (ferromanganese nodules) through x-ray fluorescence satellite analysis has been proposed as an alternative to the laborous and time-consuming volumetric method [33]. Attention has also been focused in the speciation of platinum in order to control its activity in alumina-based catalysts intended to reform gasoline fractions in modern oil refining, by measuring the Pt satellite intensity ratios of the L- and M-series lines [34]. More recently, Wang *et al.* [35] demonstrated that shake-up satellites in x-ray photoelectron spectroscopy can be used to localize the interfaces associated with biomolecules deposited on top of bioelectronic devices

[*]Contact author: slimandri@unc.edu.ar

grown on silicon semiconductors, which is crucial in the ulterior performance of these hybrid systems.

In this work, satellite lines in the high-energy neighborhood of $M\alpha$ and $M\beta$ diagram transitions induced by electron irradiation are studied. To this aim, expressions for the estimation of satellite intensities associated with one and two spectator holes originated in AU and CK transitions and those associated with one spectator hole SH processes are furnished in Sec. II. To provide a quantitative example, these expressions are applied to characterize the fine-structure observed in Re $M\alpha$ and $M\beta$ emissions; the results are then compared with the experimental data in x-ray emission spectra induced by electron bombardment, after a careful spectral processing routine [36], which allows to obtain all the satellite structure parameters: intensities, energies, and widths.

II. EXPRESSIONS FOR DIAGRAM AND SATELLITE INTENSITIES

With the aim of characterizing the x-ray spectra originated in $3s$, $3p$, and $3d$ vacancies, a complete model has been developed accounting for the emission of diagram peaks and also of satellite lines, with the aid of the ionization distribution function $\varphi(\rho z)$. Following the notation presented in Ref. [37], the present approach is based on the assumption of an electron beam of energy E_o impinging upon a flat bulk monoelemental sample with atomic mass A and density ρ.

A. Diagram lines

The emitted intensity I_ν^{P} for a diagram line associated with a particular transition ν, corresponding to a radiative decay from a W_j shell to a Y_i shell ($\nu \equiv W_j \to Y_i$), may be expressed in terms of the number of incident electrons n_e, the fluorescence yield ω_{Y_i} for the Y_i shell (total probability for radiative decays to a single Y_i hole), and the transition rate P_ν, i.e., the relative radiative probability for this ν decay. This probability involves not only the contributions arising in the direct Y_i-shell ionization, but also those associated with the ionization of other inner shells which result in Y_i-shell vacancies through a possible mechanism for atom relaxation. These contributions are determined by the initial X_k-shell ionization cross section σ, the corresponding ionization distribution function $\varphi_{X_k}(\rho z)$ with mass depth ρz, and the transition rates which transfer the vacancy from X_k to Y_i. To obtain the intensity I_ν^{P}, the attenuation of the ν photons within the sample must be also taken into account. With these ideas in mind, it is useful to define the integral

$$\mathbb{I}_{X_k}^{\nu} = \int_0^\infty \varphi_{X_k}(\rho z) e^{-\chi^\nu \rho z} d\rho z, \tag{1}$$

where $\chi^\nu = \mu_\nu / \sin\theta$, with θ being the take-off angle, and μ_ν, the x-ray mass absorption coefficient at the ν emission energy [38]. This integral may be expressed considering the Gaussian model for the function $\varphi(\rho z)$, which involves the parameters a, b, γ, and ϕ [39,40], as well as the R fifth-order polynomial estimate for the complementary error function [41], obtaining

$$\mathbb{I}^{\nu} = \frac{\gamma\, R\left(\frac{\chi^\nu}{2a}\right) - (\gamma - \phi)\, R\left(\frac{b+\chi^\nu}{2a}\right)}{a}. \tag{2}$$

Hence, the intensity I_ν^{P} may be written as

$$I_\nu^{\mathrm{P}} \equiv n_e \frac{N_A}{A} \omega_{Y_i} P_\nu \times \left[\sigma_{Y_i} \mathbb{I}_{Y_i}^{\nu} + \sum_{X_k} \sigma_{X_k} \mathbb{I}_{X_k}^{\nu} \{X_k \xrightarrow{\mathrm{rad}} Y_i\} \right], \tag{3}$$

where N_A is Avogadro's number and $\{X_k \xrightarrow{\mathrm{rad}} Y_i\}$ represents the summation of all probabilities for the primary vacancy transfer from the X_k shell to the Y_i shell through radiative transitions. For example, $\{M_4 \xrightarrow{\mathrm{rad}} M_5\}$ involves a unique term, equal to the transition rate for the M_4M_5 radiative decay; instead, $\{M_3 \xrightarrow{\mathrm{rad}} M_5\}$ contains two terms: the direct radiative transition M_3M_5, and a two-step term M_3M_4 and M_4M_5.

Henceforth, decays to M-shell vacancies will be considered, taking into account that the beam energies involved in this work cannot produce primary ionizations in the K shell, but only in L_i or M_i shells. Specifically, for the subshell $Y_i = M_5$, which gives rise to the $M\alpha \equiv N_{6,7} \to M_5$ emission, the bracket in Eq. (3) results

$$\begin{aligned}
\tilde{I}_\alpha^{\mathrm{P}} &= \sigma_{M_5} \mathbb{I}_{M_5}^{\alpha} + \sum_{X_k} \sigma_{X_k} \mathbb{I}_{X_k}^{\alpha} \{X_k \xrightarrow{\mathrm{rad}} M_5\} \\
&= \sigma_{M_5} \mathbb{I}_{M_5}^{\alpha} + \sigma_{M_4} \mathbb{I}_{M_4}^{\alpha} \{M_4 \xrightarrow{\mathrm{rad}} M_5\} \\
&\quad + \sigma_{M_3} \mathbb{I}_{M_3}^{\alpha} \{M_3 \xrightarrow{\mathrm{rad}} M_5\} + \sigma_{M_2} \mathbb{I}_{M_2}^{\alpha} \{M_2 \xrightarrow{\mathrm{rad}} M_5\} \\
&\quad + \sigma_{M_1} \mathbb{I}_{M_1}^{\alpha} \{M_1 \xrightarrow{\mathrm{rad}} M_5\} + \sigma_{L_3} \mathbb{I}_{L_3}^{\alpha} \{L_3 \xrightarrow{\mathrm{rad}} M_5\} \\
&\quad + \sigma_{L_2} \mathbb{I}_{L_2}^{\alpha} \{L_2 \xrightarrow{\mathrm{rad}} M_5\} + \sigma_{L_1} \mathbb{I}_{L_1}^{\alpha} \{L_1 \xrightarrow{\mathrm{rad}} M_5\}.
\end{aligned} \tag{4}$$

Thus, $\tilde{I}_\alpha^{\mathrm{P}}$ has the same units as the ionization cross section. An analog expression may be written for the $M\beta \equiv N_6 \to M_4$ line.

B. Satellite lines associated with spectator holes

Radiative transitions arising from multiple-vacancy initial states give rise to satellite lines, generally bearing energies slightly greater than the associated diagram line. In the present work, two different mechanisms are considered for the generation of these multiple-hole states: on the one hand, Coster-Kronig and Auger transitions; and on the other hand, shake-up and shake-off processes. In this section, the calculations corresponding to each of these contributions will be introduced.

1. Coster-Kronig and Auger satellite lines

In an AU or CK transition, a vacancy is transferred from one shell or subshell to another, along with the emission of an outer electron, which, in turn, leaves a spectator hole behind. When the inner-shell vacancy is filled through a radiative decay, a satellite line is emitted whose energy depends on the spectator hole level and is slightly greater than that of the parent line. With the aim of simplifying notation, the satellites associated with the ν transition in the presence of one or two spectator holes created through an AU or CK event will be referred to as $I_\nu^{\rm CK}$, which can be written as

$$I_\nu^{\rm CK} = n_e \frac{N_A}{A}\omega_{Y_i} P_\nu \left(\sum_q \tilde{I}^{\rm CK}_{\nu_q} + \sum_{q,q'} \tilde{I}^{\rm CK}_{\nu_{qq'}}\right), \tag{5}$$

where q and q' identify those levels in which the spectator holes occur. In this expression, the probability for a ν transition in the presence of one (ν_q) or two ($\nu_{qq'}$) spectator holes (given by the product of the corresponding fluorescence yield and transition rate) is assumed not to be affected by the presence of spectator holes, and may be expressed as $(\omega_{Y_i} P_\nu)$. Considering the emission of an $M\alpha$ photon, a final vacancy in the M_5 shell can be produced along with a q-level spectator hole, through a CK or AU transition to a primary vacancy in levels L_{1-3} or M_{1-4}, or also through the combination of CK or AU and radiative transitions between two of these levels. Similarly, a final vacancy in the M_5 shell may occur accompanied by two spectator holes in levels q and q', through the combination of two successive nonradiative transitions complemented with radiative decays, which will transfer the primary vacancy from an L_{1-3} or M_{1-3} level towards the M_5 shell. Each term of the summations in Eq. (5) thus becomes

$$\begin{aligned}\tilde{I}^{\rm CK}_{\alpha_q} = {} & \sigma_{M_4}\mathbb{I}^{\alpha_q}_{M_4}\{M_4 \xrightarrow{q} M_5\} + \sigma_{M_3}\mathbb{I}^{\alpha_q}_{M_3}\{M_3 \xrightarrow{q} M_5\} \\ & + \sigma_{M_2}\mathbb{I}^{\alpha_q}_{M_2}\{M_2 \xrightarrow{q} M_5\} + \sigma_{M_1}\mathbb{I}^{\alpha_q}_{M_1}\{M_1 \xrightarrow{q} M_5\} \\ & + \sigma_{L_3}\mathbb{I}^{\alpha_q}_{L_3}\{L_3 \xrightarrow{q} M_5\} + \sigma_{L_2}\mathbb{I}^{\alpha_q}_{L_2}\{L_2 \xrightarrow{q} M_5\} \\ & + \sigma_{L_1}\mathbb{I}^{\alpha_q}_{L_1}\{L_1 \xrightarrow{q} M_5\},\end{aligned} \tag{6}$$

and

$$\begin{aligned}\tilde{I}^{\rm CK}_{\alpha_{qq'}} = {} & \sigma_{M_3}\mathbb{I}^{\alpha_{qq'}}_{M_3}\{M_3 \xrightarrow{qq'} M_5\} \\ & + \sigma_{M_2}\mathbb{I}^{\alpha_{qq'}}_{M_2}\{M_2 \xrightarrow{qq'} M_5\} + \sigma_{M_1}\mathbb{I}^{\alpha_{qq'}}_{M_1}\{M_1 \xrightarrow{qq'} M_5\} \\ & + \sigma_{L_3}\mathbb{I}^{\alpha_{qq'}}_{L_3}\{L_3 \xrightarrow{qq'} M_5\} + \sigma_{L_2}\mathbb{I}^{\alpha_{qq'}}_{L_2}\{L_2 \xrightarrow{qq'} M_5\} \\ & + \sigma_{L_1}\mathbb{I}^{\alpha_{qq'}}_{L_1}\{L_1 \xrightarrow{qq'} M_5\}.\end{aligned} \tag{7}$$

Here $\{X_k \xrightarrow{q} M_5\}$ or $\{X_k \xrightarrow{qq'} M_5\}$ represent the summation of all probabilities for transferring the primary vacancy from the X_k to the M_5 shell leaving whether one spectator hole in the q level or two spectator holes in q, q' levels, respectively. A set of expressions similar to Eqs. (6) and (7) are obtained for the $M\beta$ decay.

2. Shake-up and shake-off satellite lines

Inner-shell ionizations may give rise to shake processes due to the sudden change in the atom core potential. In these processes, the atomic electrons have certain probability to be excited to an unoccupied bound state (shake-up) or ejected to the continuum (shake-off), leaving a spectator hole in the atom. It is worth mentioning that the probability for the occurrence of such processes depends on the ejected electron kinetic energy.

The intensity associated with a transition ν in the presence of a spectator hole arising from a shake-up or shake-off (SH) process may be expressed as

$$I_\nu^{\rm SH} = n_e \frac{N_A}{A}\omega_{Y_i} P_\nu \left(\sum_q \tilde{I}^{\rm SH}_{\nu_q}\right), \tag{8}$$

where

$$\tilde{I}^{\rm SH}_{\nu_q} = \sigma_{Y_i}\xi_q \mathbb{I}^{\nu_q}_{Y_i}$$

and ξ_q stands for the shake probability associated with level q.

Summarizing, from Eqs. (3) to (8) and assuming that the emitted intensity for the diagram line $I_\nu^{\rm P}$ is due to the direct ionization of the shell Y_i, i.e., the terms with $\{X_k \xrightarrow{\rm rad} Y_i\}$ can be neglected in Eq. (3), the total intensity for the ν line (diagram and satellite contributions included) can be condensed as

$$\begin{aligned}I_\nu = n_e \frac{N_A}{A}\omega_{Y_i} P_\nu \Bigg[& \left(1 - \sum_q \xi_q\right)\tilde{I}_\nu^{\rm P} \\ & + \sum_q \left(\tilde{I}^{\rm CK}_{\nu_q} + \tilde{I}^{\rm SH}_{\nu_q}\right) + \sum_{q,q'} \tilde{I}^{\rm CK}_{\nu_{qq'}}\Bigg].\end{aligned} \tag{9}$$

III. EXPERIMENTAL AND SPECTRAL PROCESSING

X-ray emission spectra for Re $M\alpha$ and $M\beta$ lines were obtained from a set of pure bulk standards (SPI Supplies). Since the standards are embedded in a nonconductive resin within a steel block, a carbon coating was used to ensure adequate conductivity. The thickness of the carbon layer was determined by analyzing a spectrum measured from a silicon standard, which is located close to the Re target used, and a value of (42 ± 1) nm was obtained from the spectral fit performed by means of the software POEMA [36].

The target was irradiated with electrons of incident energies $\tilde{E}_o = 20$, 10, 5, 3, and 2.55 keV, using beam currents in the range 178 to 290 nA, in a LEO 1450 VP scanning electron microscope. To account for the attenuation in the carbon layer, the procedure detailed in Ref. [42] was followed. The resulting effective incident energies E_o were 19.93, 9.87, 4.74, 2.59, and 2.09 keV. The x-ray spectra induced in this way were measured with the PET crystal of an INCA WAVE 700 wavelength dispersive spectrometer (WDS) in a Johansson-type arrangement, the take-off angle being 29°.

All the spectra analyzed here were fitted by using a robust spectral processing tool previously developed and implemented in the above-mentioned software POEMA [36]. The spectral processing method consists in fitting a function to the experimental data, by optimizing the instrumental and atomic parameters involved in the analytical description. The latter mainly consists of a term for the bremsstrahlung and additional terms for the peaks; as detailed elsewhere [43], for the present spectrometer resolution under electron bombardment, diagram lines are modeled by Voigt profiles, whereas satellite structures are better represented by Gaussian functions since they may involve multiple emissions.

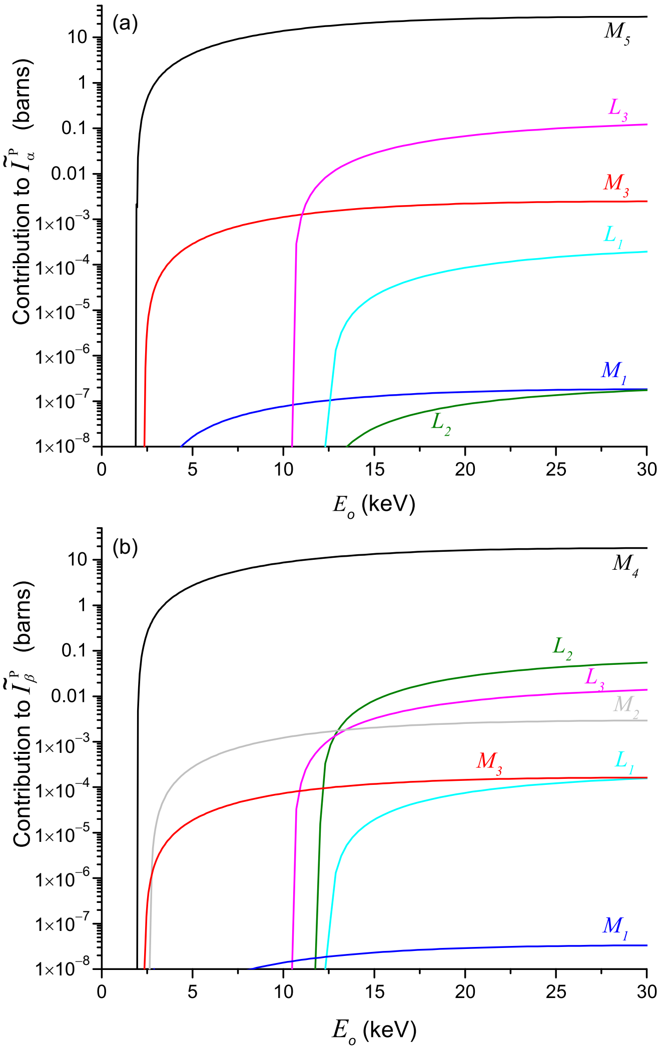

FIG. 1. Contribution to the (a) $\tilde{I}^{\mathrm{P}}_{\alpha}$ and (b) $\tilde{I}^{\mathrm{P}}_{\beta}$ Re intensities due to the generation of primary vacancies in shells M_5 and M_4 (direct ionization, in black); M_3 (red); M_2 (gray); M_1 (blue); L_3 (magenta); L_2 (green); and L_1 (cyan).

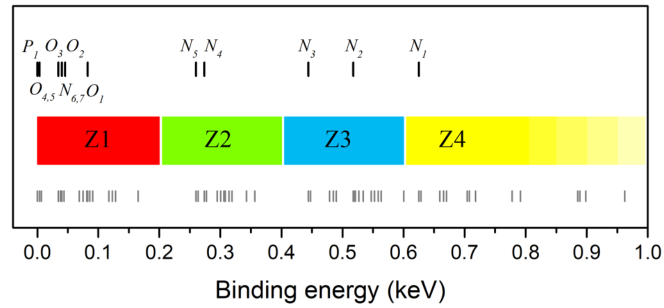

FIG. 2. Satellite lines grouped according to the Re atomic binding energies where spectator holes occur. Black sticks: atom level energies. Gray sticks: addition of atomic level pairs. The color bars identify groups Z1 to Z4, as indicated along the text.

IV. RESULTS AND DISCUSSION

A. Calculations for Re

Figure 1 displays the contributions to $\tilde{I}^{\mathrm{P}}_{\alpha}$ [Eq. (4)] and $\tilde{I}^{\mathrm{P}}_{\beta}$ in the case of Re due to primary vacancies occurring in the different shells, assessed by means of the transition rates reported by Perkins *et al.* [21], along with the ionization cross sections given by Bote *et al.* [44]. It can be seen that the contributions originated in primary ionizations from shells other than the M_5 amount less than 0.4% for all beam energies considered along this work, which suggests they can be neglected in a first approximation. Particularly, M_2 and M_4 subshells produce null contributions to the $M\alpha$ emission.

1. *Grouping of satellite lines*

When analyzing the satellite energies, it is reasonable to accept that the more inner the spectator hole level is, the more important the atom perturbation will be, which implies a stronger shift of the satellite emission towards higher energies. For double vacancies, these shifts may be associated with the addition of the vacancy level energies. Concurring with this idea, Fig. 2 displays the binding energies corresponding to the levels where the vacancies may occur for Re. Each black stick represents a level energy for single spectator holes, whereas gray sticks stand for the addition of pairs of these energies, taking the values reported by Bearden and Burr [45]. As can be seen, some levels bear values very close to others, which suggests that the respective satellite lines would have similar energies and can be grouped. Following this criterion, four groups have thus been defined. Z1 (red) corresponds to transitions in the presence of spectator holes with energy levels below 200 eV; this group is associated with the satellite structure closest to the diagram line. The Z2 group (green) embraces vacancy levels between 200 and 400 eV. The Z3 group (blue) ranges from 400 to 600 eV, and the Z4 group (yellow) involves energies greater than 600 eV, associated with those satellite lines more departed from the main emission. Notice that the holes in P_1 and $O_{4,5}$ were included for completeness, although they produce satellite lines with energies practically indistinguishable from the parent line.

It is worth mentioning that the assumption regarding the suggested relationship between the satellite energy shifts and the binding energy associated with the spectator hole is generally appropriate when comparing spectator vacancies with different main and orbital quantum numbers. Although a more detailed analysis involving spin-spin or spin-orbit coupling might provide further insight, the consequent variations are expected to be small compared to the width of the zones defined for grouping the satellite lines.

2. *Relative intensities of satellite lines*

The intensity contributions to satellite lines due to CK processes given in Eqs. (6) and (7) for $M\alpha$ have been assessed similarly to those corresponding to the primary intensities (Eq. (4), also using the transition rates provided by Ref. [21], and the cross sections assessed following [44]). Since the energy differences between satellite and diagram lines are small ($<$20 eV) and no absorption edges occur in this energy interval, the mass attenuation coefficients μ_{α_q} and $\mu_{\alpha_{qq'}}$ can be approximated by μ_{α}. It is worth pointing out that, for two spectator holes in the same level ($q = q'$), transition rates are expected to deviate from those associated with single

TABLE I. Contributions to the Re $M\alpha$ satellite line intensities due to the presence of one spectator hole in the atomic level q generated by CK transitions, for 20 keV incident electrons. The colors identify the satellite energy zones (Z1: red; Z2: green; Z3: cyan; Z4: yellow), while their brightness indicates the relative importance of each contribution. The hollow boxes correspond to transitions with probabilities less than 1%.

Zone	1 hole q							
Z1	N_6	N_7	O_1	O_2	O_3	O_4	O_5	P_1
Z2				N_4	N_5			
Z3				N_3	N_2			
Z4				N_1				

TABLE III. Contributions to the satellite lines intensities associated with the transition $M\beta$ for Re due to the presence of one spectator hole in the level q at 20 keV. Color code: See Table I.

Zone	1 hole q							
Z1	N_6	N_7	O_1	O_2	O_3	O_4	O_5	P_1
Z2				N_4	N_5			
Z3				N_2	N_3			
Z4				N_1				

vacancies; to account for this issue, the CK yields associated with the second spectator hole were corrected multiplying it by a factor $(n-1)/n$, where n is the number of electrons in the considered level for a neutral atom. Tables I and II display the Zi zones containing the transitions associated with one or two spectator holes in the different levels q, q'. Each zone is identified with its color (as described in the previous section), the intensities of these colors indicating the relative importance of each contribution, as obtained for the case of a 20-keV electron beam.

For each energy zone, Fig. 3 displays the CK contribution of satellite intensities associated with the presence of one or two spectator holes, originated in initial L and M vacancies. These contributions are described by the corresponding terms in Eqs. (6) and (7). It is worth noticing that L initial vacancies can be neglected since they amount, at most, to two orders of magnitude below the main contributions. In energy regions closer to the main emission (Z1, Z2, and Z3), satellite intensities are mainly due to the presence of spectator holes initially originated in a M_3 primary vacancies. In region Z1, the contribution due to spectator holes transferred from the M_4 shell is also important, and it is the only one below 2.37 keV (M_3 edge). The remaining contributions, arising from initial vacancies in other shells, is below 7% (Z1), 20% (Z2), and 26% (Z3), with some important shares from two-spectator hole processes. The satellite energies most distant from the main peak do not involve contributions originating in M_3-shell primary vacancies; moreover, the main shares are due to one or two spectator holes arising from the M_1 shell, these contributions bearing quite similar magnitudes.

In the case of the $M\beta$ emission, the transitions originated in primary M_2 vacancies are, in general, the most influential, along with the corresponding to the M_3 subshell for the Z2 zone (see Tables III and IV, and also Fig. 4). Instead of the increasing behavior of the $M\alpha$ group satellite intensities with the incident energy E_o (Fig. 3), those corresponding to the $M\beta$ group (Fig. 4) stabilize after a certain value. In fact, when E_o increases, more ionizations are produced, and consequently, more satellite emissions; however, the interaction volume within the irradiated material also increases leading to a stronger self-absorption of the emitted radiation, which is more important for the $M\beta$ group since the M_5 absorption edge value lies between the $M\beta$ diagram and satellite lines [46]. Figures 3 and 4 suggest that these two effects compensate each other in the case of $M\beta$ lines, but not in the case of

TABLE II. Contributions to the Re $M\alpha$ satellite line intensities due to the presence of two spectator holes in the atomic levels q, q' for 20-keV incident electrons. The color code is the same as in Table I. Only pairs q, q' are shown since the matrix is symmetric.

$q\backslash q'$	N_1	N_2	N_3	N_4	N_5	N_6	N_7	O_1	O_2	O_3	O_4	O_5	P_1
N_1	Z4	Z4	Z4	Z4	Z4	Z4	Z4	Z4	Z4	Z4	Z4	Z4	Z4
N_2		Z4	Z4	Z4	Z4	Z3	Z3	Z4	Z3	Z3	Z3	Z3	Z3
N_3			Z4	Z4	Z4	Z3	Z3	Z3	Z3	Z3	Z3	Z3	Z3
N_4				Z3	Z3	Z2	Z2	Z2	Z2	Z2	Z2	Z2	Z2
N_5					Z3	Z2	Z2	Z2	Z2	Z2	Z2	Z2	Z2
N_6						Z1	Z1	Z1	Z1	Z1	Z1	Z1	Z1
N_7							Z1	Z1	Z1	Z1	Z1	Z1	Z1
O_1								Z1	Z1	Z1	Z1	Z1	Z1
O_2									Z1	Z1	Z1	Z1	Z1
O_3										Z1	Z1	Z1	Z1
O_4											Z1	Z1	Z1
O_5												Z1	Z1
P_1													Z1

TABLE IV. Contributions to the satellite lines intensities associated with the transition $M\beta$ for Re due to the presence of two spectator holes in the levels q, q' at 20 keV. The color code is the same as in Tables I and II.

$q\backslash q'$	N_1	N_2	N_3	N_4	N_5	N_6	N_7	O_1	O_2	O_3	O_4	O_5	P_1
N_1	Z4	Z4	Z4	Z4	Z4	Z4	Z4	Z4	Z4	Z4	Z4	Z4	Z4
N_2		Z4	Z4	Z4	Z4	Z3	Z3	Z4	Z3	Z3	Z3	Z3	Z3
N_3			Z4	Z4	Z4	Z3	Z3	Z3	Z3	Z3	Z3	Z3	Z3
N_4				Z3	Z3	Z2	Z2	Z2	Z2	Z2	Z2	Z2	Z2
N_5					Z3	Z2	Z2	Z2	Z2	Z2	Z2	Z2	Z2
N_6						Z1	Z1	Z1	Z1	Z1	Z1	Z1	Z1
N_7							Z1	Z1	Z1	Z1	Z1	Z1	Z1
O_1								Z1	Z1	Z1	Z1	Z1	Z1
O_2									Z1	Z1	Z1	Z1	Z1
O_3										Z1	Z1	Z1	Z1
O_4											Z1	Z1	Z1
O_5												Z1	Z1
P_1													Z1

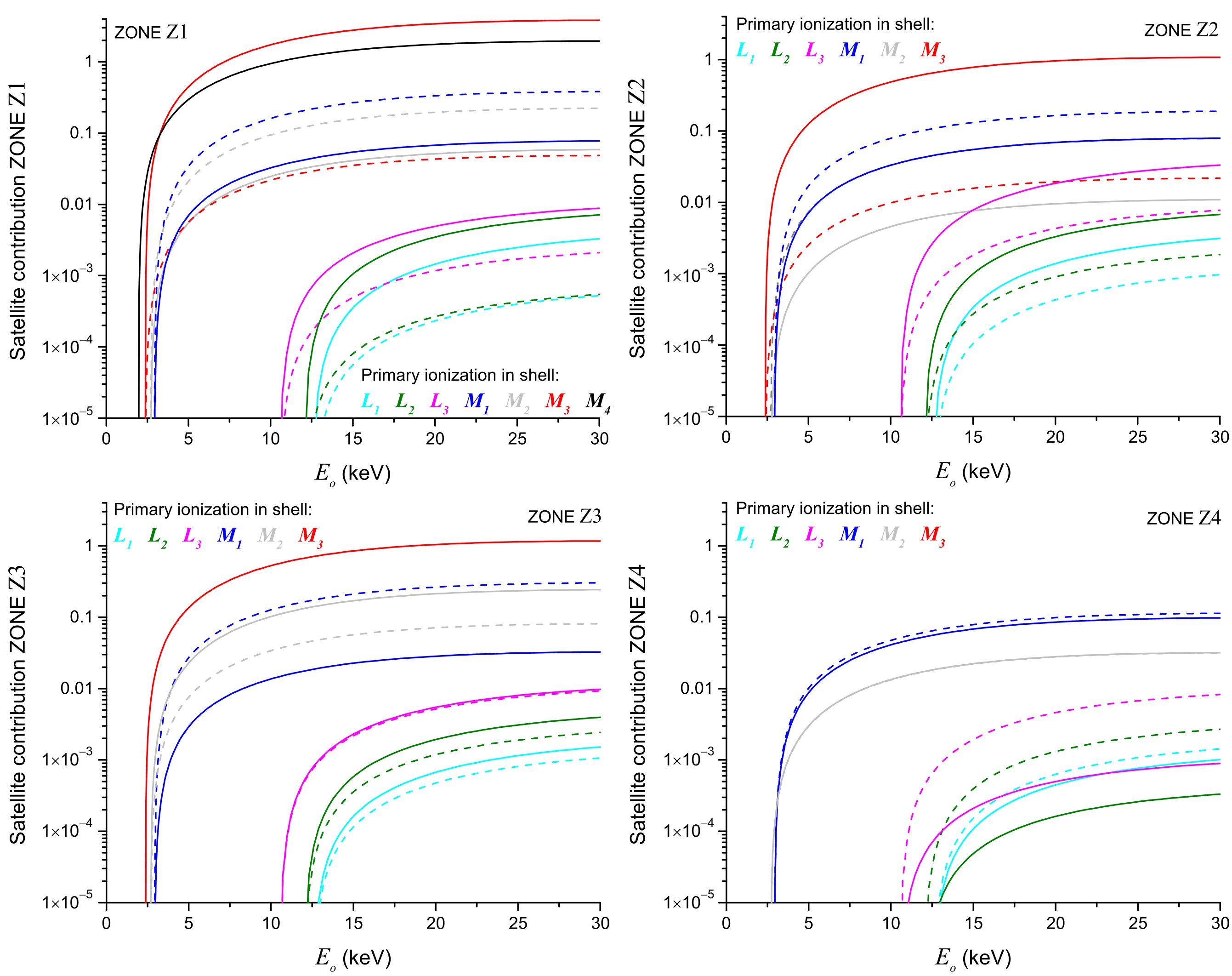

FIG. 3. Contribution to the satellite intensities for the Re $M\alpha$ line associated with the presence of one spectator hole (solid lines) and two spectator holes (dashed lines) originated from primary vacancies in shells M_4 (black), M_3 (red), M_2 (gray), M_1 (blue), L_3 (magenta), L_2 (green), and L_1 (cyan). The intensities are plotted versus the incidence energy.

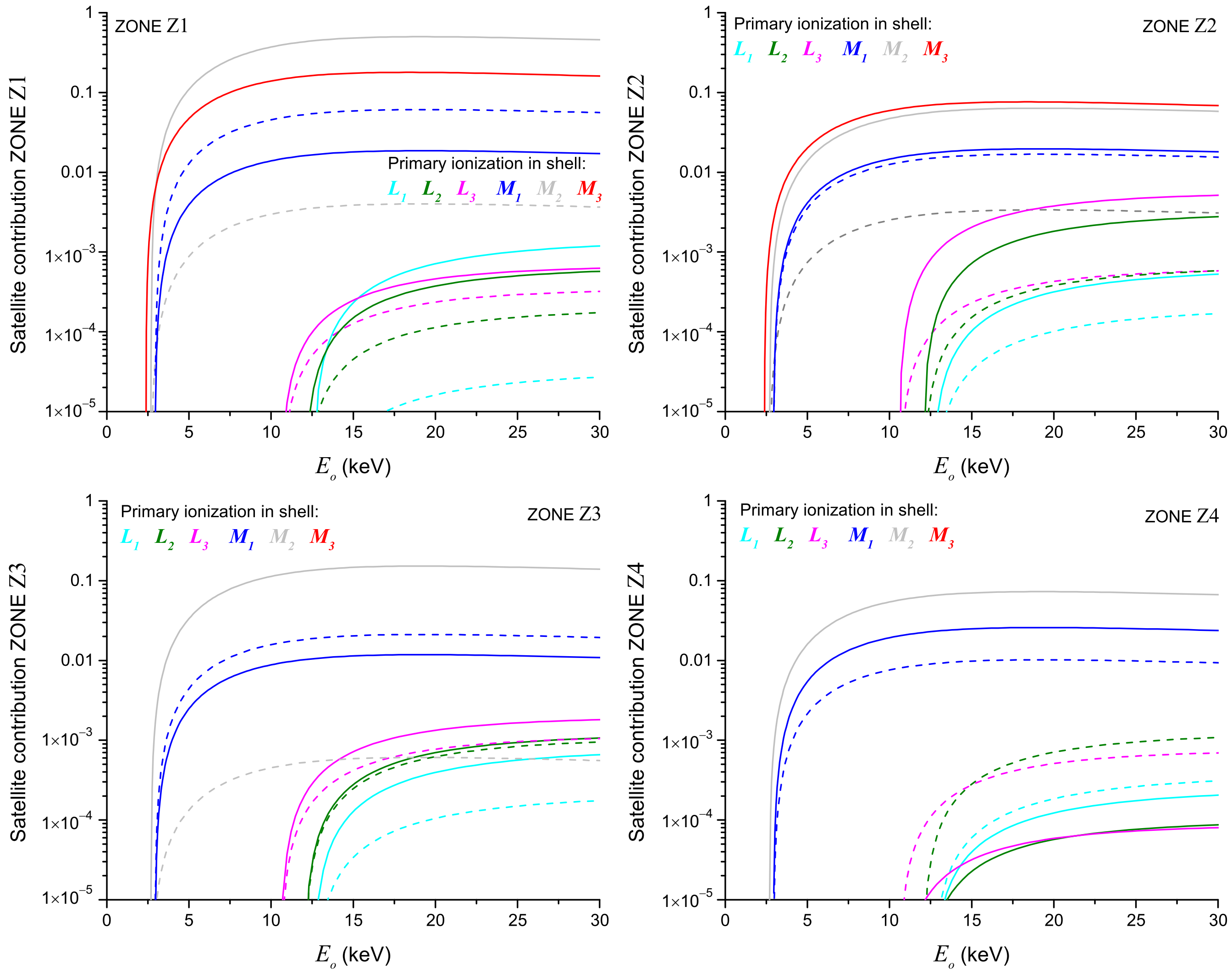

FIG. 4. Contribution to the satellite intensities for Re $M\beta$ line associated with the presence of one spectator hole (solid lines) and two spectator holes (dashed lines) originated from primary vacancies in shells M_3 (red), M_2 (gray), M_1 (blue), L_3 (magenta), L_2 (green), and L_1 (cyan). The intensities are plotted versus the incidence energy.

$M\alpha$: the M_5 absorption edge imposes a strong absorption for satellite $M\beta$ lines, but not for the parent $M\beta$ emission.

Regarding the shake contributions to the satellite intensities, to the best of the authors' knowledge there exist only two databases to look up and assess the shakeup or shakeoff probabilities ξ_q for Re, both corresponding to theoretical calculations within the sudden approximation. Carlson *et al.* [26] reported calculations for ξ_q in several elements of the periodic table using Hartree-Fock-Slater wave functions (nonrelativistic for lighter elements and relativistic for heavier ones), and interpolated for other elements. Their results are independent from the atomic shell hosting the primary vacancy; although they correspond to β decays, these authors assert they are also valid for external electron irradiation. Another approach offered by Mukoyama [27] reported shake probabilities corresponding to vacancies in the different M_i subshells, on the basis of relativistic calculations by using Dirac-Fock-Slater wave functions. Table V displays the percent probabilities for Re, as obtained from interpolations within the values reported in both works. As can be seen, the values for M_4

TABLE V. Electron shake probabilities (%) for Re. Values obtained by interpolation of the data given by Mukoyama [27] for sudden vacancy creation in shells M_4 (a) and M_5 (b), and Carlson *et al.* [26]. Value marked with ∗ corresponds to an interpolation of data calculated by the authors but in a range not interpolated by them.

q	Mukoyama[a]	Mukoyama[b]	Carlson *et al.*
N_1	0.017	0.017	0.170
N_2	0.027	0.026	0.179
N_3	0.060	0.058	0.297
N_4	0.146	0.135	0.350
N_5	0.293	0.289	0.504
N_6	1.490	1.487	1.138
N_7	1.940	1.932	1.480
O_1	0.130	0.130	0.385
O_2	0.340	0.340	0.688
O_3	0.868	0.860	1.470
O_4	7.270	7.260	
P_1	5.510	5.500	6.8*

TABLE VI. Values obtained for the $S_{\nu,i}$ coefficients defined in Eq. (10), representing the satellite intensity fraction corresponding to each Zi group.

	$S_{\alpha,1}$		$S_{\alpha,2}$		$S_{\alpha,3}$		$S_{\alpha,4}$		$S_{\beta,1}$		$S_{\beta,2}$		$S_{\beta,(3,4)}$	
E_o (keV)	CK	SH	CK	SH	CK	SH	CK	SH	CK	SH	CK	SH	CK	SH
19.932	0.546	0.122	0.122	0.020	0.151	0.011	0.024	0.004	0.327	0.360	0.079	0.060	0.129	0.045
9.865	0.548	0.131	0.117	0.022	0.145	0.012	0.021	0.004	0.380	0.297	0.090	0.049	0.146	0.038
4.738	0.547	0.156	0.106	0.025	0.130	0.014	0.017	0.005	0.374	0.311	0.091	0.051	0.136	0.039
2.591	0.515	0.311	0.040	0.052	0.043	0.028	0.000	0.011	0.067	0.700	0.029	0.116	0.000	0.088
2.086	0.469	0.397	0.000	0.077	0.000	0.043	0.000	0.015	0.000	0.776	0.000	0.128	0.000	0.096

and M_5 shells provided by Mukoyama are quite similar, the differences being lower than 1%. However, important differences between these two authors occur, particularly for shells which are assigned very low probabilities ($N_{1\text{-}5}$ y $O_{1,2}$). The most influential shells contributing to shake processes are $N_{6,7}$, $O_{3,4}$, and P_1. Regarding the O_4 shell, it is worth noticing that Carlson *et al.* [26] reported values only starting from $Z = 79$; an extrapolating exponential function provides a value of 9.6% for Re. In the case of the O_5 shell, the authors present no values in the atomic number range of interest, an estimate for Re not being possible since anomalies may occur for incompletely filled shells. Finally, although these authors assigned an important shake contribution to the P_1 shell, the corresponding satellite emission energy associated with a hole in this shell is expected to be experimentally indistinguishable from the diagram line since its binding energy is almost zero: its intensity will therefore be attached to the main decay.

From these data, if the P_1-shell contribution is excluded, the shake probability estimate for shake lies between 12 and 16%. Something similar can be stated for the $O_{4,5}$-shell contribution since these binding energies are rather low (see Fig. 2). If their satellite contribution is also disregarded, the shake probability reduces to 5 to 7%. Bearing in mind that the CK contributions from these shells are rather unimportant within the corresponding zone (see Tables II to IV), instead of adding them to the satellite intensity, they were associated with the primary line.

At this point, it is useful to define the satellite intensity ratios $S_{\nu,i}$, referred to the total satellite intensity $I_\nu^{\text{CK}} + I_\nu^{\text{SH}}$, for the corresponding Zi zone:

$$S_{\nu,i} = \frac{\sum_{q\in Zi}\left(\tilde{I}^{\text{CK}}_{\nu_q} + \tilde{I}^{\text{SH}}_{\nu_q}\right) + \sum_{q,q'\in Zi}\tilde{I}^{\text{CK}}_{\nu_{qq'}}}{\sum_{q}\left(\tilde{I}^{\text{CK}}_{\nu_q} + \tilde{I}^{\text{SH}}_{\nu_q}\right) + \sum_{q,q'}\tilde{I}^{\text{CK}}_{\nu_{qq'}}}. \tag{10}$$

Table VI displays the contributions to the ratios $S_{\nu,i}$ from the CK (with one and two holes) and SH terms assessed at the E_o values in the range of interest of the present work, using the probabilities obtained from Carlson *et al.* [26] for the shake contributions. It must be mentioned that, for the $M\beta$ satellite group, only three zones are included since, in this case, the last region involves the transitions belonging to the Z3 and Z4 groups, as explained in Sec. IV B. For incident energies above 4 keV, both contributions vary slightly in each energy zone, and the SH share is quite lower than that of the CK, excepting for the Z1 region associated with the $M\beta$ group, where they are similar. For lower energies, closer to the absorption edges, the corresponding cross sections strongly decrease, the intensity furnished by CK terms consequently vanishing. The only contribution to satellite intensities would therefore originate in SH processes, but it must be borne in mind that, as advised by the different authors, all these probabilities are valid within the sudden approximation, and in this energy range the corresponding hypotheses may not be valid.

It is worth mentioning that the assessments shown rely on different fundamental parameters, some of which are scarcely available in the literature, and not very recent. All the trends obtained for the satellite intensities appear to be reasonable; it would be interesting, however, to count on updated theoretical calculations for these parameters by means of modern atomic computation software packages, such as GRASP [47], FAC [48], or JAC [49].

B. Experimental characterization for Re

Bearing in mind the expression given by Eq. (9), the analytical function I proposed to describe the experimental spectrum can be written as

$$I = I_B + \sum_\nu C_\nu\left[(1-\delta)V_\nu + \delta\sum_i S^*_{\nu,i}G_{\nu,i}\right], \tag{11}$$

where I_B stands for the continuum spectrum, the first summation involves the three diagram lines considered along this work ($\nu = \alpha_1,\ \alpha_2,\ \beta$), C_ν is a parameter related to the multiplying factors in Eq. (9), in which the detection efficiency has also been included, δ is a parameter optimized to match the total satellite contributions, V_ν and $G_{\nu,i}$ are functions of the photon energy accounting for the corresponding peak shape: a Voigt function for diagram lines, and a Gaussian profile to describe satellite emissions, respectively; finally, the parameter $S^*_{\nu,i}$ = is defined as $S_{\nu,i}/C_\nu$.

Figure 5 shows examples for the predictions attained in spectra measured for pure Re at different beam energies, where the diagram peaks are discriminated from the satellite contributions, for the sake of clarity. It can be seen that the final fittings bear a very good quality, even in those cases where the experimental statistics was rather low (for extremely low overvoltages).

The Voigt and Gaussian peak functions mentioned above depend on two parameters, namely, the peak width and its centroid, which allows for the characterization of the position of the corresponding lines. Particularly, four satellite lines are considered for the $M\alpha$ group (identifying them with the corresponding energy zones defined above), whereas only three were necessary for the description of the $M\beta$ structure, following the criterion of minimizing the number of lines used

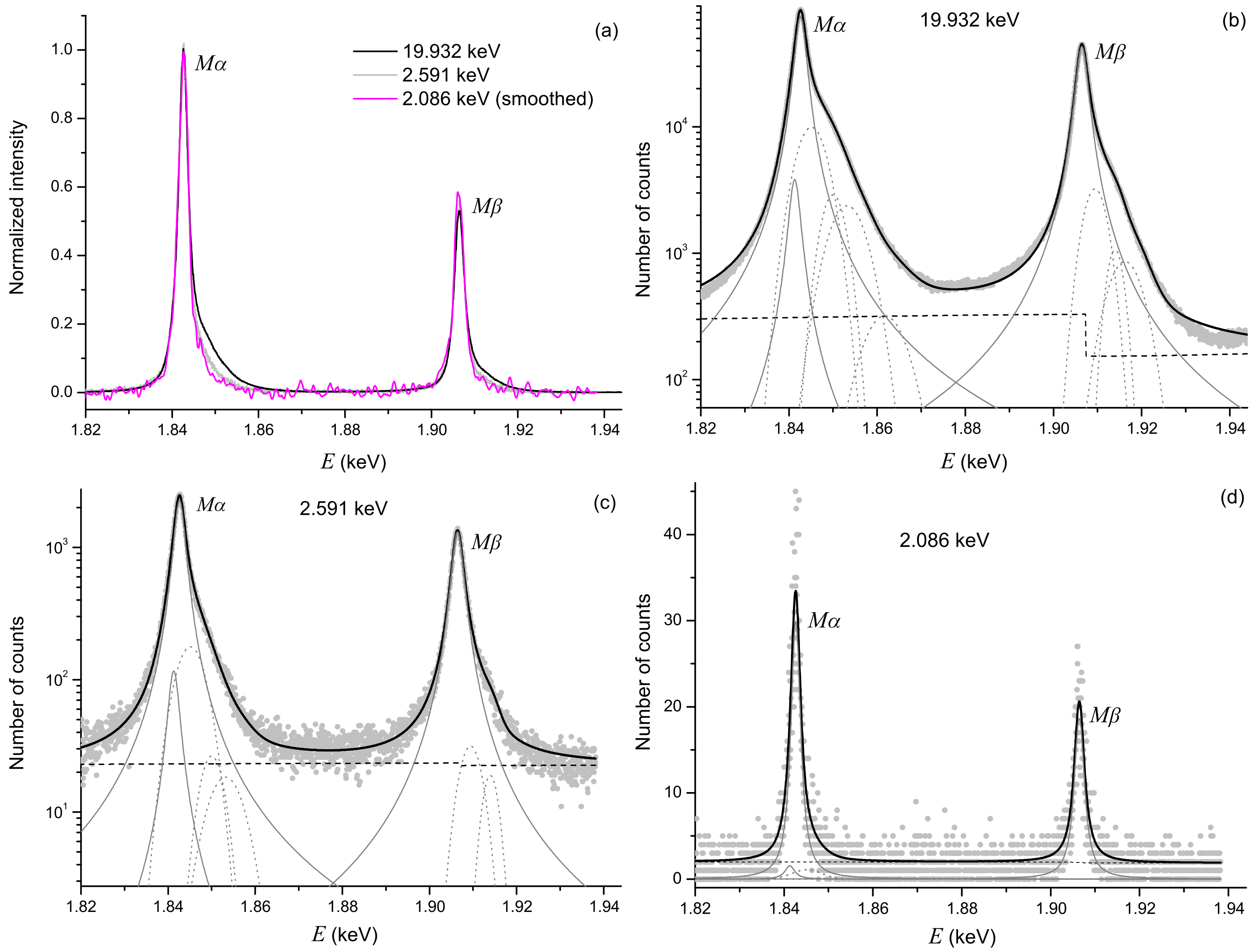

FIG. 5. Rhenium M-line WDS spectra. (a) Experimental spectra normalized to the $M\alpha$ maxima. Spectral fitting for (b) 19.932-, (c) 2.591-, and (d) 2.086-keV electrons, along with the measured intensities. Dots: experimental; solid black line: fit; solid gray line: diagram transitions; dashed gray line: satellite transitions; dashed black line: background.

for the fitting. The convenience of this zone identification choice relies in the fact that if two or more decays bear sufficiently close energy values, it is rather difficult or even impossible to provide a reliable separation not only because of the natural width associated with these transitions, but also due to the instrumental widening always present in the detection process.

In the optimization routines carried out, the spectrometer gain and zero calibration parameters were refined by considering, as mentioned above, Voigt profiles to describe characteristic lines, in this case two for $M\alpha_1$ and $M\alpha_2$ separately, and one more for the $M\beta$ decay. The combined $M\alpha$ group energy was kept equal to the value published by Bearden [50], the following requirements being imposed to this aim: on the one hand, the doublet $M\alpha_{1,2}$, assessed as a weighted average with the radiative transition probabilities given by Perkins *et al.* [21], must agree with the value reported by Bearden, and on the other hand, the difference between $M\alpha_1$ and $M\alpha_2$ must coincide with the difference of the corresponding values given by Perkins *et al.*

The 20-keV spectrum was chosen as starting point for the parameter refinement pursued, to take advantage of the better statistics it exhibited. In this case, the $M\alpha_2$ and $M\beta$ line energies, as well as the natural widths for $M\alpha_1$ and $M\beta$ decays, were obtained through the optimization procedure; instead, for the natural width for the weaker $M\alpha_2$ emission, the value obtained for $M\alpha_1$ was successively adopted. In addition, all satellite energies along with the corresponding widths were optimized, the values obtained for all these magnitudes being transferred as fix parameters to the remaining spectra. As a final step in the optimization process, the calibration gain and the zero offset were refined for each spectrum, as well as the bremsstrahlung scale factor [51], the instrumental broadening and the C_ν and δ factors of Eq. (11).

It is worth clarifying that the peak areas obtained in these fittings correspond to detected photons, whereas Eq. (9) represents emitted photons. For this reason, it was necessary to apply the corresponding correction to the experimental intensities recorded, to appropriately account for the detector efficiency, which was assessed according to a method previously developed [52].

Table VII displays the widths for the Gaussian functions $G_{\nu,i}$ obtained, and also the energy shifts relative to the diagram line associated. It is worth mentioning that, even maintaining

TABLE VII. Energy shift from the diagram line and Gaussian widths for the satellite lines, as obtained from the optimization process applied to the 20-keV spectrum.

	$G_{\alpha,1}$	$G_{\alpha,2}$	$G_{\alpha,3}$	$G_{\alpha,4}$	$G_{\beta,1}$	$G_{\beta,2}$	$G_{\beta,3,4}$
Rel. energy (eV)	2.9	7.9	10.8	19.1	3.6	8.2	10.9
Width (eV)	8.1	6.9	10.4	12.0	6.4	4.6	8.5

the intensity ratios obtained in Table VI as constant in the optimization process, the energy shifts obtained for the satellite lines preserve the order foreseen in the present approach.

Bearing in mind that satellite peaks involve several lines each, their widths are expected to maintain certain relationship with the spreading in the sticks depicted in Fig. 2. For regions Z1, Z2, and Z3, this spreading is almost the scattering of the energy levels (black sticks in Fig. 2) since the contribution due to two spectator holes (gray sticks in Fig. 2) is quite lower, as can be observed in Figs. 3 and 4. In region Z4 instead, the $M\alpha$-line analysis must also include the combination of two levels (gray sticks in Fig. 2) since two-spectator holes bear an important contribution in this group, as can be inferred from Fig. 3.

From the data displayed in Table VII, it can be seen that the satellite line widths obtained after the optimization process maintain the expected trend. In fact, in the case of $M\alpha$ lines, the satellite structure $G_{\alpha,4}$ is observed to become the widest, whereas the $G_{\alpha,2}$ is the narrowest; the remaining two structures bear intermediate widths, as already observed in Fig. 2. Regarding the $M\beta$ lines, the $G_{\beta,2}$ is the narrowest and the $G_{\beta,3}$, the widest, which also reproduces the trend shown in the mentioned figure.

Figure 6 shows the total satellite intensity F_{sat}, relative to the total emission (parent diagram line plus satellites). The continuous curves represent the $M\alpha$ and $M\beta$ predictions from Sec. II, according to Eqs. (3) to (9), where the $O_{4,5}$ and P_1 contributions are excluded from the SH term, as discussed above. The full circles stand for the experimental ratios, obtained with the peak areas resulting after the spectral refinement process described above. As can be seen, the theoretical curves follow the experimental data general trend when both SH and CK mechanisms are taken into account. It is worth mentioning that, in the case of the $M\beta$ group, the self-absorption effects are quite more important than in the $M\alpha$ case; particularly, the attenuation coefficients involved in expression (1) may correspond to the energy interval embraced by the M_5 absorption edge structure.

V. CONCLUSION

Satellite intensities have been carefully depicted for $M\alpha$ and $M\beta$ transitions in heavy elements, providing detailed expressions for the CK terms corresponding to single and double spectator hole states, as well as for shake-up and shake-off emissions. As an illustrative example, this approach was applied for the case of Re, for which different energy zones were defined in the vicinity of the main peaks. In the case of $M\alpha$ emission, in energy regions close to the main emission (Z1, Z2, and Z3), satellite intensities are mainly due to the presence of spectator holes initially originated in M_3 primary vacancies; in addition, the contribution due to spectator holes transferred from the M_4 shell is also important in region Z1 (see Fig. 3). For the $M\beta$ emissions, the transitions with spectator holes in the M_2 subshell (and also in M_3 subshell for the Z2 zone) are the most influential (see Fig. 4). The most remarkable

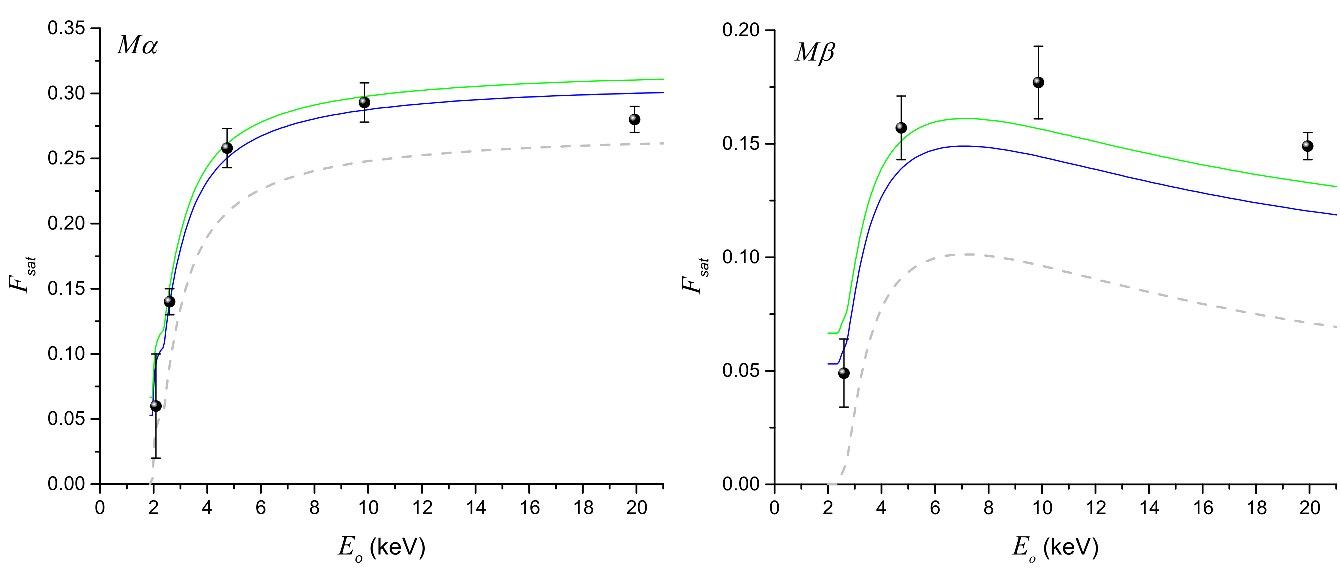

FIG. 6. Satellite intensities associated with the $M\alpha$ (left) and $M\beta$ (right) transitions, relative to the total intensity. Experimental results (full circles); calculations with SH probabilities given by Mukoyama [27] (blue) and Carlson *et al.* [26] (green). The pure CK contribution is plotted with dashed line.

difference arising in the dependence of the associated intensities on the incident beam energy: in the case of the $M\beta$ satellite lines, their intensities stabilize above certain E_o value, unlike the $M\alpha$ group, in which a monotonically increasing trend is observed (a contrasting behavior because of the distinct self-absorption effects).

The good agreement evidenced between the experimental relative intensities for Re and those assessed from the expressions derived supports the approach presented in this work. Particularly, both the proportion of satellite intensities in each group and satellite-to-diagram ratios have proven to lead to appropriate spectral descriptions matching the experimental data. Complementary, these optimization routines with the POEMA software [36], subsequently applied to a set of experimental WDS spectra induced by electron irradiation, allowed to assess the $M\alpha$ and $M\beta$ satellite emission energies.

The knowledge of satellite intensity ratios would doubtlessly benefit if the experimental study carried out along the present work was complemented by using modern computation software packages [47–49], intended for full atomic theoretical calculations.

ACKNOWLEDGMENTS

This work was financially supported by the Secretaría de Ciencia y Técnica of the Universidad Nacional de Córdoba (UNC, Argentina), and also through a PIP2021 Grant No. 11220200100986CO (CONICET, Argentina). The authors are also grateful to the Laboratorio de Microscopía Electrónica y Microanálisis (LABMEM-UNSL) where the measurements were performed.

[1] G. Rémond, R. Myklebust, M. Fialin, C. Nockolds, M. Phillips, and C. Roques-Carmes, J. Res. Natl. Inst. Stand. Technol. **107**, 509 (2002).
[2] T. Åberg, in *Atomic Inner-Shell Processes*, edited by B. Crasemann (Academic Press, New York, 1975), Chap. 9.
[3] D. S. Urch, J. Phys. C **3**, 1275 (1970).
[4] G. Rémond, C. Gilles, M. Fialin, O. Rouer, R. Marinenko, R. Myklebust, and D. Newbury, in *Microbeam and Nanobeam Analysis*, edited by D. Benoit, J. F. Bresse, L. Van't dack, H. Werner, and J. Wernisch, Mikrochimica Acta Supplement Vol. 13 (Springer, Vienna, 1996), pp. 61–86.
[5] T. Mukoyama, X-Ray Spectrom. **45**, 263 (2016).
[6] J. W. Dean, S. Thompson, and C. Chantler, Molecules **29**, 4199 (2024).
[7] J. W. Dean, H. A. Melia, T. V. B. Nguyen, and C. T. Chantler, Phys. Rev. A **109**, 022809 (2024).
[8] W. Jitschin, G. Materlik, U. Werner, and P. Funke, J. Phys. B **18**, 1139 (1985).
[9] U. Werner and W. Jitschin, Phys. Rev. A **38**, 4009 (1988).
[10] W. Jitschin, G. Grosse, and P. Röhl, Phys. Rev. A **39**, 103 (1989).
[11] S. L. Sorensen, R. Carr, S. J. Schaphorst, S. B. Whitfield, and B. Crasemann, Phys. Rev. A **39**, 6241 (1989).
[12] S. L. Sorensen, S. J. Schaphorst, S. B. Whitfield, B. Crasemann, and R. Carr, Phys. Rev. A **44**, 350 (1991).
[13] R. Stotzel, U. Werner, M. Sarkar, and W. Jitschin, J. Phys. B: At. Mol. Opt. Phys. **25**, 2295 (1992).
[14] H. J. Sánchez, R. D. Pérez, M. Rubio, and G. Castellano, X-Ray Spectrom. **24**, 221 (1995).
[15] R. A. Barrea, C. A. Pérez, and H. J. Sánchez, J. Phys. B: At. Mol. Opt. Phys. **35**, 3167 (2002).
[16] R. A. Barrea, C. A. Pérez, and H. J. Sánchez, Spectrochim. Acta Part B At. Spectrosc. **57**, 999 (2002).
[17] A. Kumar, S. Puri, D. Mehta, M. L. Garg, and N. Singh, X-Ray Spectrom. **31**, 103 (2002).
[18] R. A. Barrea, C. A. Pérez, and H. J. Sánchez, Spectrochim. Acta Part B At. Spectrosc. **58**, 51 (2003).
[19] W. Cao, J. Hoszowska, J.-C. Dousse, Y. Kayser, M. Kavčič, M. Žitnik, K. Bučar, A. Mihelič, J. Szlachetko, and K. Słabkowska, Phys. Rev. A **80**, 012512 (2009).
[20] W. Bambynek, B. Crasemann, R. W. Fink, H. U. Freund, H. Mark, C. D. Swift, R. E. Price, and P. V. Rao, Rev. Mod. Phys. **44**, 716 (1972).
[21] S. T. Perkins, D. E. Cullen, M. H. Chen, J. H. Hubbell, J. Rathkopf, and J. H. Scofield, Lawrence Livermore National Laboratory Report No. UCRL-50400 30, 1 (1991).
[22] E. McGuire, Phys. Rev. A **5**, 1043 (1972).
[23] S. Poonia and S. Soni, J. Electron Spectrosc. Relat. Phenom. **122**, 27 (2002).
[24] C. Couratin, P. Velten, X. Fléchard, E. Liénard, G. Ban, A. Cassimi, P. Delahaye, D. Durand, D. Hennecart, F. Mauger, A. Méry, O. Naviliat-Cuncic, Z. Patyk, D. Rodríguez, K. Siegień-Iwaniuk, and J.-C. Thomas, Phys. Rev. Lett. **108**, 243201 (2012).
[25] X. Fabian, X. Fléchard, B. Pons, E. Liénard, G. Ban, M. Breitenfeldt, C. Couratin, P. Delahaye, D. Durand, P. Finlay, B. Guillon, Y. Lemière, F. Mauger, A. Méry, O. Naviliat-Cuncic, T. Porobic, G. Quéméner, N. Severijns, and J.-C. Thomas, Phys. Rev. A **97**, 023402 (2018).
[26] T. A. Carlson, C. W. Nestor, T. C. Tucker, and F. B. Malik, Phys. Rev. **169**, 27 (1968).
[27] T. Mukoyama, X-Ray Spectrom. **44**, 7 (2015).
[28] T. Mukoyama, X-Ray Spectrom. **52**, 226 (2023).
[29] J. Kawai, *X-Ray Spectroscopy for Chemical State Analysis* (Springer Nature, Singapore, 2023), pp. 63–105.
[30] M. J. Jercinovic and M. L. Williams, Am. Mineral. **90**, 526 (2005).
[31] M. J. Jercinovic, M. L. Williams, and E. D. Lane, Chem. Geol. **254**, 197 (2008).
[32] K. Müller, G. S. Majkic, and J. K. Meen, IEEE Trans. Appl. Supercond. **25**, 1 (2015).
[33] V. Chubarov, Minerals **13**, 1329 (2023).
[34] V. M. Chubarov, A. L. Finkelshtein, and S. A. Skornikova, Spectrochim. Acta Part B At. Spectrosc. **209**, 106803 (2023).
[35] S. Wang, J. Guo, H. Shen, X. Li, C. Cen, S. Cai, and M. Deng, ChemPhysChem **25**, e202400436 (2024).
[36] R. Bonetto, G. Castellano, and J. Trincavelli, X-Ray Spectrom. **30**, 313 (2001).
[37] A. Carreras, G. Castellano, S. Segui, and J. Trincavelli, Phys. Rev. A **102**, 012817 (2020).

[38] C. T. Chantler, J. Phys. Chem. Ref. Data **29**, 597 (2000).
[39] R. Packwood and J. Brown, X-Ray Spectrom. **10**, 138 (1981).
[40] J. A. Riveros and G. E. Castellano, X-Ray Spectrom. **22**, 3 (1993).
[41] M. Abramowitz and I. Stegun, *Handbook of Mathematical Functions*, 9th ed., (Dover, New York, 1970), p. 299.
[42] S. Limandri, A. Carreras, and J. Trincavelli, Microsc. Microanal. **16**, 583 (2010).
[43] F. Fernandez, A. Sepúlveda, S. Limandri, J. Trincavelli, and G. Castellano, Phys. Rev. A **108**, 052826 (2023).
[44] D. Bote, F. Salvat, A. Jablonski, and C. Powell, At. Data Nucl. Data Tables **95**, 871 (2009).
[45] J. A. Bearden and A. F. Burr, Rev. Mod. Phys. **39**, 125 (1967).
[46] J. Trincavelli, G. Castellano, S. Segui, S. Limandri, M. del Rosario Torres Deluigi, C. Montanari, D. Mitnik, and A. Carreras, Phys. Rev. A **109**, 042804 (2024).
[47] C. Froese Fischer, G. Tachiev, G. Gaigalas, and M. R. Godefroid, Comput. Phys. Commun. **176**, 559 (2007).
[48] M. F. Gu, Can. J. Phys. **86**, 675 (2008).
[49] S. Fritzsche, Comput. Phys. Commun. **240**, 1 (2019).
[50] J. A. Bearden, Rev. Mod. Phys. **39**, 78 (1967).
[51] G. Castellano, J. Osán, and J. Trincavelli, Spectrochim. Acta, Part B At. Spectrosc. **59**, 313 (2004).
[52] J. Trincavelli, S. Limandri, A. Carreras, and R. Bonetto, Microsc. Microanal. **14**, 306 (2008).